GEOPHYSICS. VOL. 76, NO. 6 (NOVEMBER-DECEMBER 2011); P. WC181–WC198, 20 FIGS., 6 TABLES.
10.1190/GEO2011-0064.1

Investigation of injection-induced seismicity using a coupled fluid flow and rate/state friction model

Mark W. McClure[1] and Roland N. Horne[1]

ABSTRACT

We describe a numerical investigation of seismicity induced by injection into a single isolated fracture. Injection into a single isolated fracture is a simple analog for shear stimulation in enhanced geothermal systems (EGS) during which water is injected into fractured, low permeability rock, triggering slip on preexisting large scale fracture zones. A model was developed and used that couples (1) fluid flow, (2) rate and state friction, and (3) mechanical stress interaction between fracture elements. Based on the results of this model, we propose a mechanism to describe the process by which the stimulated region grows during shear stimulation, which we refer to as the sequential stimulation (SS) mechanism. If the SS mechanism is realistic, it would undermine assumptions that are made for the estimation of the minimum principal stress and unstimulated hydraulic diffusivity. We investigated the effect of injection pressure on induced seismicity. For injection at constant pressure, there was not a significant dependence of maximum event magnitude on injection pressure, but there were more relatively large events for higher injection pressure. Decreasing injection pressure over time significantly reduced the maximum event magnitude. Significant seismicity occurred after shut-in, which was consistent with observations from EGS stimulations. Production of fluid from the well immediately after injection inhibited shut-in seismic events. The results of the model in this study were found to be broadly consistent with results from prior work using a simpler treatment of friction that we refer to as static/dynamic. We investigated the effect of shear-induced pore volume dilation and the rate and state characteristic length scale, d_c. Shear-induced pore dilation resulted in a larger number of lower magnitude events. A larger value of d_c caused slip to occur aseismically.

INTRODUCTION

Overview

Enhanced geothermal systems (EGS) are characterized by the use of hydraulic stimulation to increase flow rate in high temperature, low productivity wells, most often located in crystalline rock. Water is typically injected at high pressure without proppant. In most cases, the elevated fluid pressure triggers slip on preexisting fractures. The process of using elevated fluid pressure to trigger fracture slip is often referred to as "shear stimulation." When the fractures slip, their permeability is permanently enhanced, and well productivity can be improved by an order of magnitude or more (Tester, 2007).

An important challenge for the deployment of EGS is that shear stimulation triggers microseismicity, low magnitude seismic events that sometimes can be felt at the surface (Majer et al., 2007). Induced seismicity threatens public acceptance of EGS, and the possibility of triggering a truly damaging seismic event, while seemingly remote, deserves careful consideration. In 2005, one of the largest seismic events ever associated with an EGS project, a magnitude 3.4 earthquake, occurred following the hydraulic stimulation of an EGS well in Basel, Switzerland. As a result, the project was suspended and eventually canceled (Häring et al., 2007; Majer et al., 2007). Events strong enough to be felt at the surface have occurred during stimulations at several other EGS projects, including at Soultz-sous-Forêts, France, magnitude 2.9, and Cooper Basin, Australia, magnitude 3.7 (Majer et al., 2007).

There is a practical need for credible shear stimulation modeling because shear stimulation directly impacts induced seismicity,

Manuscript received by the Editor 15 February 2011; revised manuscript received 11 May 2011; published online 6 January 2012; corrected version published online 23 January 2012.
[1]Stanford University, Stanford Geothermal Program Department of Energy Resources Engineering, Stanford, California, USA. E-mail: mcclure@stanford.edu, horne@stanford.edu.

well productivity, and the long term temperature decline of the system. Shear stimulation and induced seismicity modeling have applications in areas outside of EGS, including gas shale hydraulic fracturing and carbon dioxide sequestration.

Shear stimulation models typically include (1) stochastic or deterministic generation of a preexisting fracture network, (2) simulation of fluid flow in the network, and (3) modeling of induced slip (Willis-Richards et al., 1996; Rahman et al., 2002; Ghassemi and Tarasovs, 2006; Kohl and Mégel, 2007; Bruel, 2007; Baisch et al., 2010; McClure and Horne, 2010; Rachez and Gentier, 2010; Deng et al., 2011).

Significant issues remain in the development of shear stimulation modeling. The complexity of the physical processes taking place and the uncertainty and incompleteness of the data forces modelers to make significant simplifying assumptions. Two physical phenomena that are frequently subject to simplifying assumptions are fracture friction and stresses induced by fracture slip. A more detailed discussion of these topics can be found in Appendix A, "Seismicity modeling in EGS."

A goal of the shear stimulation modeling described in this paper was to focus on realistic treatment of friction and induced stresses. Rate and state theory was used to describe fracture friction. Rate and state friction is based on laboratory observations of rock friction and has been successful in describing a variety of earthquake phenomena (Dieterich, 2007; Segall, 2010). Stress interaction was calculated using the Crouch and Starfield (1983) boundary element method which assumes that the rock material is homogenous, isotropic, and linearly elastic. These assumptions are reasonable for EGS reservoirs that are located in fractured granite.

Injection into a single, isolated, 1D fracture was modeled. The problem geometry was simple, but it was a reasonable analog for injection into faulted granite such as is found at the EGS project at Soultz-sous-Forêts, France. At Soultz, observations suggested that flow and seismicity was confined to a small number of large scale faults. A more detailed discussion can be found in Appendix B, "Relationship of our model to actual EGS reservoirs."

Summary of results

Major results of this paper are summarized in this section. Many of the results were consistent with what has been described by other studies in the literature. There were several results that are novel and could have important practical implications.

The mechanism of growth of the stimulated region was a two-part cycle. The cycle began with a seismic event that spread slip and permeability enhancement into a region of the fracture where slip had not previously occurred and where there was low permeability and fluid pressure. The second part of the cycle was flow of water into the newly slipped patch of fracture, which eventually triggered the next seismic event. We refer to this process as the "sequential stimulation" (SS) mechanism.

The SS mechanism is distinctly different from a process that has been described in the literature in which pressure diffuses into unstimulated fracture regions, subsequently causing slip (Bruel, 2007). We refer to this process as the "diffusion controlled" (DC) mechanism.

The difference is that in the DC mechanism, slip follows pressure diffusion. In the SS mechanism, pressure diffusion follows slip. SS behavior will only occur in a model if stress interaction between elements is included and friction is allowed to weaken (as it would during a seismic event). SS behavior is not unique to rate and state friction models, as similar behavior was described in McClure and Horne (2010) using an instantaneously weakening friction model that we refer to as static/dynamic.

If the SS, not the DC, mechanism controls the growth of the stimulated region, it would undermine several common assumptions. In the literature, unstimulated hydraulic diffusivity has been estimated using the assumption that it controls the rate of growth of the stimulated region during injection (Shapiro et al., 1999; Bruel, 2007). In the SS mechanism, the rate of growth of the stimulated region during injection does not depend on the unstimulated diffusivity.

The SS mechanism could explain why injection pressure tends to increase only slightly when injection rate is increased during shear stimulation. Previously, such behavior has been interpreted as being caused by the opening of tensile fractures at a pore pressure equal to the least principal stress (Cornet and Bérard, 2003; Valley and Evans, 2007; Cornet et al., 2007). The SS mechanism provides an alternative explanation that does not involve the propagation of opening mode tensile fractures and does not require the pore pressure to be equal to the least principal stress. The least principal stress would be underestimated if it was assumed incorrectly to be equal to the pore pressure during injection.

In the model, spreading and redistribution of pressure after the end of injection caused shut-in seismicity, a commonly observed phenomenon in which seismic events of significant magnitude continue to occur at the edge of the stimulated region after shut-in (Häring et al., 2007; Asanuma et al., 2006; Baisch et al., 2010). Redistribution of pressure has also been proposed as a mechanism for shut-in events by Baisch et al. (2006), Healy et al. (1968), and Hsieh and Bredehoeft (1981).

We investigated strategies to minimize induced seismicity. Reducing injection pressure over time reduced the maximum magnitude. With constant injection pressure over time, using a lower injection pressure led to fewer significant sized events, but did not affect the maximum magnitude. Producing fluid back after injection reduced shut-in seismicity. Baisch et al. (2006) also suggested producing fluid could reduce shut-in events.

We investigated the effect of two geological uncertainties on the results, namely pore volume dilation during slip and the value of the rate and state characteristic length scale, d_c. A larger d_c caused slip to occur aseismically as opposed to seismically. Pore volume dilation caused slip to occur with a larger number of lower magnitude events. Both results were consistent with other studies in the literature (Ruina, 1983; Yamashita, 1999; Segall and Rice, 1995; Segall et al., 2010).

METHODS

Problem definition

Our numerical model required solution of five equations for five primary variables. The variables were velocity (v), state (θ), mass of fluid in a cell (m), shear traction (τ), and cumulative shear displacement (D). A full list of symbols is given in Table 1. The equations solved were unsteady-state fluid mass balance (with Darcy's law), frictional force equilibrium (with a radiation damping approximation term), a stress strain relationship that related shear displacement to shear traction, the aging law for state evolution, and the time integral relationship between slip velocity and cumulative shear displacement.

The problem was solved on a 1D fracture embedded in a 2D homogenous, isotropic medium. It was assumed that the permeability of the surrounding medium was zero (reasonable for fractures embedded in granite), and so the injected water was located only in the fracture.

The 2D stress/strain problems were solved using plane stress, which assumes the thickness of the medium in the third dimension is infinite. For some calculations, an infinite height fracture would lead to unrealistic results. For example, an infinite height fracture would have an infinite flow rate. Therefore, for calculations not involving stress and strain, fracture height was defined to be b_w, which we set to 100 m.

The simulations were isothermal. The fluid was single-phase liquid water.

The unsteady-state fluid mass balance equation in a fracture is (Aziz and Settari, 1979; with fracture aperture E replacing porosity)

$$\frac{\partial(\rho E)}{\partial t} = \nabla q + s, \tag{1}$$

where q is the mass flux rate, s is a source term, t is time, E is the void aperture (the pore volume per cross-sectional area of fracture), and ρ is the fluid density. Darcy flow was assumed, in which mass flow across an area A in a direction x_i is (Aziz and Settari, 1979)

$$q = \frac{k\rho A}{\mu}\frac{\partial P}{\partial x_i}, \tag{2}$$

where P is fluid pressure, μ is fluid viscosity, and k is permeability.

The permeability k is given by the "cubic law" and defined as (Jaeger et al., 2007)

$$k = \frac{e^2}{12}, \tag{3}$$

where e is hydraulic aperture, which is the effective aperture for flow in the fracture. Hydraulic aperture is equal to void aperture between two smooth plates, but can be lower than void aperture between rough surfaces such as a rock fracture.

For flow in a 1D fracture, the cross-sectional area A is $b_w * e$, and so the mass flow rate is

$$q = \frac{\rho b_w e^3}{12\mu}\frac{\partial P}{\partial x_i}. \tag{4}$$

For a closed fracture, force equilibrium requires that shear traction be equal to the frictional resistance to slip. An additional term, $v * \eta$, called the radiation damping term, can be included to approximate the damping effect of inertia on sliding at high velocities (Rice, 1993). The variable η is on the order of one to tens of

Table 1. Table of symbols.

v	Sliding velocity	t	Time
θ	State	T	Stress tensor
m	Mass of fluid in cell	G	Shear modulus
τ	Shear traction	v_p	Poisson's ratio
σ_n	Normal traction	ε	Strain tensor
σ_n'	Effective normal traction	I	Unit matrix
D	Cumulative shear displacement	E_0	Void aperture constant
b_w	Out-of-plane width	e_0	Hydraulic aperture constant
E	Void aperture	E_{res}	Residual void aperture
q	Mass flux rate	e_{res}	Residual hydraulic aperture
ρ	Fluid density	D_{emax}	Maximum hydraulic aperture displacement
A	Area	D_{Emax}	Maximum void aperture displacement
P	Fluid pressure	σ_{Enref}	Void aperture reference normal traction
k	Permeability	σ_{enref}	Hydraulic aperture reference normal traction
μ	Fluid viscosity	$\varphi_{\text{Edil(1,2)}}$	Void aperture dilation angle
s	Mass source term	$\varphi_{\text{edil(1,2)}}$	Hydraulic aperture dilation angle
e	Hydraulic aperture	M_0	Seismic moment
η	Radition damping coefficient	M_w	Moment magnitude
μ_f	Coefficient of friction	B	Matrix of sliding to shear traction interaction coefficients
f_0	Nominal coefficient of friction	P_{inj}	Injection pressure
v_0	Velocity normalizing constant	P'_{inj}	Injection pressure derivative
a	Velocity effect coefficient	μ_s	Static coefficient of friction from S/D friction
b	State effect coefficient	μ_d	Dynamic coefficient of friction from S/D friction
d_c	Characteristic displacement scale	T_{inj}	Injection temperature
σ^r_{yy}	Remote compressive stress in the y-direction	T_{init}	Initial temperature
σ^r_{xy}	Remote shear stress	σ^r_{xx}	Remote compressive stress in the x-direction

MPa/(m/s), which means that the radiation damping term is negligible for $v \ll 1$ m/s. The frictional equilibrium equation is (Segall, 2010):

$$\tau - \eta v = \mu_f \sigma_n^{'}, \tag{5}$$

where μ_f is the coefficient of friction and σ_n' is the effective normal traction, defined as (Segall, 2010)

$$\sigma_n^{'} = \sigma_n - P \tag{6}$$

where compressive tractions are taken to be positive. Following the rate and state friction law, the coefficient of friction is defined as a function of sliding velocity and state (Segall, 2010)

$$\mu_f = f_0 + a \ln \frac{v}{v_0} + b \ln \frac{\theta v_0}{d_c}, \tag{7}$$

where f_0, v_0, a, b, and d_c are material constants. The variable d_c is referred to as the characteristic displacement scale. The parameters a and b are ~0.01, much smaller than f_0, which is ~0.6. Their relatively small value is consistent with the observation that only a fraction of the stress borne by a fracture is usually released during a seismic event.

Under a rate and state framework, all fractures are slipping at all times. Fractures can have a tiny slip velocity. Very tiny velocities are physically meaningless on the time scale of a hydraulic stimulation, but that is not a practical difficulty because these fractures behave approximately as if locked.

The state variable can be interpreted as the average contact time of asperities on the fault. The "aging law" of state evolution is (Segall, 2010)

$$\frac{\partial \theta}{\partial t} = 1 - \frac{\theta v}{d_c}. \tag{8}$$

Dieterich (1979) associated the state variable with asperity contact time. Dieterich and Kilgore (1994) demonstrated experimentally that surface contact area increased with contact time due to creep of asperities.

The stresses induced by fracture slip were calculated according to the equations of quasistatic equilibrium in a continuum assuming that body forces are equal to zero. These stresses are given by the vector equation (Jaeger et al., 2007)

$$\nabla^T \mathrm{T} = 0, \tag{9}$$

where T is the stress tensor.

Linear elasticity in an isotropic, homogeneous body was assumed, which means that the relationship between stress and strain is given by Hooke's law (Jaeger et al, 2007)

$$T = \frac{2G\nu_p}{1 - 2\nu_p} \mathrm{trace}(\varepsilon) I + 2G\varepsilon, \tag{10}$$

where I is the unit matrix, ε is the strain tensor, ν_p is Poisson's ratio, and G is the shear modulus.

The cumulative displacement at any point is equal to the time integral of velocity

$$D = \int v \mathrm{d}t. \tag{11}$$

Void and hydraulic aperture are related to effective normal traction and cumulative displacement. There is not a universally accepted equation in the literature for the relationship between these variables. A modified version of the equation was used by Willis-Richards et al. (1996), Rahman et al. (2002), Kohl and Mégel (2007), and others was

$$E = \frac{E_0}{1 + 9\sigma_n^{'}/\sigma_{\mathrm{Enref}}} + D_1 \tan \frac{\phi_{\mathrm{Edil1}}}{1 + 9\sigma_n^{'}/\sigma_{\mathrm{Enref}}} + D_2 \tan \frac{\phi_{\mathrm{Edil2}}}{1 + 9\sigma_n^{'}/\sigma_{\mathrm{Enref}}} + E_{\mathrm{res}}, \tag{12}$$

where E_0, σ_{Enref}, E_{res}, φ_{Edil1}, and φ_{Edil2} are material constants. We allowed these constants to be different for hydraulic aperture, e, and void aperture E. In most simulations, φ_{Edil1} and φ_{Edil2} were set to zero so that there was no shear-induced pore volume dilation, only hydraulic aperture dilation.

Prior authors have used only one term for aperture enhancement from shear displacement. We used two terms to take into account the laboratory observation that hydraulic aperture of a fracture tends to increase more slowly after the initial shear displacement. Such a property was not recognized in early laboratory testing of shear displacement and aperture coupling in granite (Barton et al., 1985). More recent laboratory work has observed this phenomenon. Esaki et al. (1999) and Lee and Cho (2002) both found that for a shearing fracture in granite, permeability increased rapidly at first, but permeability increased slowly or not at all after 5–10 mm of slip. Esaki et al. (1999) and Lee and Cho (2002) both observed an increase in mechanical aperture with slip beyond 10 mm. It is not clear whether or not void aperture continued to increase after 10 mm of slip.

The parameters D_1 and D_2 were defined as follows

$$D_1 = D\,(\text{for } D < D_{\max}) \quad D_1 = D_{\max}(\text{for} D > D_{\max})$$
$$D_2 = 0(\text{for } D < D_{\max}) \quad D_2 = D - D_{\max}(\text{for } D > D_{\max}). \tag{13}$$

Fluid density and viscosity are related to fluid pressure (and temperature, but the simulations were isothermal). Values were interpolated from a large table of properties generated using the freeware Matlab code XSteam 2.6 by Magnus Holmgren (2007).

A microseismic event was considered to have begun when the maximum velocity on the fracture exceeded 5 mm/s. A slip event was considered finished when the highest velocity on the fracture dropped below 2.5 mm/s. Event durations were variable, but were at most a few seconds. Event hypocenters were defined as the location where slip velocity first exceeded 5 mm/s.

The total amount of displacement on the fracture during the event was correlated to seismic magnitude. The seismic moment M_0 is a measure of the size and energy release of an earthquake (Stein and Wysession, 2003). M_0 is defined as the integral of displacement over the fracture area times the shear modulus

$$M_0 = G \int D \mathrm{d}A. \tag{14}$$

From Hanks and Kanamori (1979), the seismic moment magnitude M_w is defined as

$$M_w = \frac{\log_{10} M_0}{1.5} - 6.06, \tag{15}$$

where M_0 is defined in N-m. For calculation of slip surface area, the dimension of the fracture out of the plane (in the third dimension) was taken to be b_w. For a one-dimensional fracture, a patch of slip dA is equal to $b_w dl$, where dl is an increment of distance along the fracture.

Modeling a 1D fracture instead of a two-dimensional fracture had some consequences, but should not have had a major impact on the overall results. Total displacements were overestimated slightly because in the 2D plane strain elastic solution, displacement goes on infinitely in the third, out-of-plane coordinate direction. Surface area close to the wellbore was overestimated because flow from the wellbore was 1D, not radial. As a result, the magnitudes of events near the wellbore were overestimated and the magnitudes of distant events were underestimated. Because the fracture in this study was 1D, the magnitudes calculated should only be compared relative to each another and not be considered actual magnitude predictions.

Finally, the dimensionality of the fracture affected connectivity with respect to heterogeneity. For fluid or slip to travel from one location to another on a 1D fracture, it has to travel through all points in between. For a 2D fracture, fluid or slip can propagate around barriers.

We neglected elastodynamic transfer of stress. Stress changes were propagated instantaneously and calculated using the quasi-static boundary element solution. Dynamic stresses may have some effect on the results, but are computationally intensive to calculate. Lapusta (2001) found for a single fracture case, calculations neglecting dynamic stresses could be made consistent with dynamic stress calculations by using a lower value of η. Lapusta suggested that for geometries more complex than a single fracture, dynamic stress transfer would play a more complicated role.

The injection well was modeled by including a source term s in the mass balance equation for the two elements at the center of the fracture. The source term for each was set to half of the total flow rate. In most simulations, injection was carried out at a specified pressure. The injection pressure was not specified directly in the model. Instead, the source term was adjusted at each time step to bring the injection pressure to the target level. The injection pressure was calculated by assuming Darcy flow between the elements adjacent to the injector and a constant pressure boundary.

In one of the simulations, fluid was produced from the wellbore at a specified rate following injection. In that case, the source term was set constant until the wellbore pressure reached the initial fluid pressure of the reservoir. At that point, production was ended.

To include some heterogeneity, the permeability of each element was multiplied by a coefficient. The coefficients did not change during the simulations and were set to be a random number between 0.1 and 2.0.

Methods of solution

The fracture was discretized into elements of constant length. The same discretization was used for the mechanical and the fluid flow parts of the problem.

The mass balance equation was solved using the finite volume method. The flow between two adjacent elements in a linear fracture was calculated from Darcy's law. The transmissibility between two elements was calculated using the harmonic average. Flow between fracture elements was calculated according to the method of Karimi-Fard et al. (2004).

The force equilibrium and stress/strain relations were solved with the 2D displacement discontinuity method, a linear elastic boundary element method (BEM) from Crouch and Starfield (1983). The problem reduces to finding the induced stresses $\Delta\tau$ at each element i caused by the cumulative shear displacements from each element j. Stresses and displacements are linearly related so that

$$\Delta\tau_i = \sum_{j=1}^{n} B_{ij} D_j \tag{16}$$

where B is a matrix of interaction coefficients calculated according to Crouch and Starfield (1983). Because the problem setup was a single, linear fracture, shear displacements only affected shear tractions, not normal tractions.

We neglected stresses induced by fracture normal displacement. The fracture in our simulations was never "open" because it never experienced tensile stress. Closed fractures can have some slight normal displacement due to loading or unloading, but these displacements are around 0.1 mm (Barton et al., 1985), and their effect should be slight compared to the effects of pore pressure change caused by injection. The fracture normal displacement in our model was around 0.1 mm.

As discussed in Appendix A, during actual EGS stimulation, injection sometimes occurs into fault zones that have much greater storativity than the crack that was used in our model. For injection of larger volumes of fluid into a fault zone, it is possible that normal traction interaction between adjacent areas of a fault could play a larger role.

Time discretization

The issue of solving mechanical and flow equations together has been discussed at length in the literature of poroelasticity. One way to solve the problem is to use implicit Euler time-stepping on every equation simultaneously and solve the entire problem as a large coupled system of equations. This is a "fully coupled" scheme (Kim et al., 2011). The fully coupled strategy is stable and accurate but is expensive computationally. We used an "explicitly coupled" scheme in which a rate and state time-step was taken, and then the time-step was repeated for the flow problem using updated values from the rate and state calculation.

The rate and state time-step was taken with an explicit, third-order Runge-Kutta scheme (Abramowitz and Stegun, 1972). In this time-step, state, shear traction, and cumulative displacement were updated. The frictional equilibrium equation, equation 5, is an algebraic constraint, not a differential equation. At the end of each substep in the Runge-Kutta scheme, the frictional equilibrium equation was solved to find velocity for each individual element. Next, a flow time-step was taken using implicit Euler to find m^{n+1}. The flow

equations and the frictional equilibrium equation were solved using Newton-Raphson iteration. Figure 1 summarizes the coupling strategy.

The advantage to splitting the problem is that different parts of the problem are most appropriately solved in different ways. The implicit Euler scheme is always numerically stable and is necessary to solve flow equations such as equation 1. However, the implicit Euler scheme requires solving a large system of equations. It would be impractical to attempt implicit Euler with the equations from the Crouch and Starfield (1983) method because the boundary element method uses a dense matrix of interaction coefficients. The matrix inversion requirements would be very large. Explicit time-steps require only multiplications of the BEM matrix.

Adaptive time-stepping was used. The time-steps were chosen based on four criteria. The first was a built-in error estimation on the calculation of state and shear traction from the third-order Runge-Kutta method. The second was the change in fluid pressure during the previous time-step. The third was the number of iterations used by the flow simulator in solving the nonlinear system of equations. The fourth was the relative amount of velocity change for each of the elements at the previous time-step. There was a target value for each criterion, and a time-step adjustment factor (either up or down) was calculated to move each value toward its target based on the result from the previous time-step. The adjustment was chosen by taking the square root of the ratio of the target to the criterion. The subsequent time-step was equal to the previous time-step multiplied by the adjustment factor. Of the four criteria, the adjustment that resulted in the most conservative time-step was used. If any of the criteria exceeded four times the target, the entire time-step was discarded and repeated with a smaller time interval.

During seismic events when slip was very rapid, very small time-steps on the order of microseconds were necessary. In between seismic events, time-steps on the order of seconds, minutes, or hours were taken.

Problem setup

Simulations were performed of injection into the center of a single, isolated, 1D fracture embedded in a 2D whole space.

The fracture was 500 m long and oriented 20° clockwise from the vertical y-axis. The 2D problem could be interpreted as viewing a strike-slip fault in plan view, a normal fault in side view, or a reverse fault in side view, rotated 90°. The fracture was discretized into 2000 elements of length 25 cm.

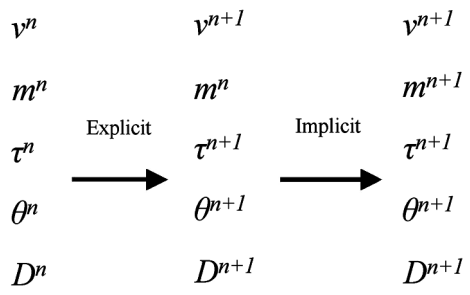

Figure 1. Explicit coupling scheme. The time-step is split into two parts. First, an explicit time-step is taken to update D, θ, and τ. Then an implicit time-step is taken to update m, and v is calculated as an algebraic constraint to enforce equilibrium.

The base case parameters are given in Table 2. T_{init} was the initial temperature and was the same as the injection temperature T_{inj}, 200 °C because the simulation was isothermal. The variables σ^r_{xx}, σ^r_{yy}, and σ^r_{xy} are the remote compressive stress in the x-direction, the y-direction, and the remote shear traction.

Once 75% of the fracture had slipped by a minimal amount, 0.1 mm, injection was ceased. The simulation was continued after injection stopped for a period equal to 20 times the duration of injection.

The frictional parameters a, b, and d_c deserve some discussion. For unstable slip to occur, a must be smaller than b (Ruina, 1983). This is because to achieve runaway velocity acceleration, the friction weakening effect of state decrease must be greater than the friction strengthening effect of velocity increase. The parameter d_c controls the minimum size of a patch of slip that can slip unstably and cause seismicity (Ruina, 1983). d_c also limits the size of the spatial discretization. The element size must be significantly smaller than a characteristic length scale related to a, b, d_c, and σ_n', otherwise the result is numerically unstable (Lapusta, 2001).

Several different simulations were carried out. The simulations were performed by specifying injection pressure. In practical EGS stimulations, positive displacement pumps are used so that the flow rate is controlled directly, not the injection pressure. However, in our simulations, trends in the injection pressure were most relevant to the behavior of the hydraulic stimulation, so injection pressure boundary conditions were used to control directly for these effects. In practice, injection pressure could be controlled indirectly by adjusting injection rate over time.

To investigate the effect of injection pressure, eight simulations were carried out using constant injection pressure (Cases A1–A8). All the simulations used pressures at 1 MPa increments from 51 MPa to 58 MPa.

To investigate the effect of decreasing injection pressure with time, 27 simulations were carried out that began with an injection pressure of 58 MPa and decreased the injection pressure over time. The injection rate was kept constant until the first microseismic event occurred, and then the injection pressure was decreased at

Table 2. List of simulation base case parameters.

P_{init}	40 MPa	D_{emax}	5 mm
T_{init}	200 °C	D_{Emax}	—
θ_{init}	10e8 s	σ_{Enref}	95 MPa
σ^r_{xx}	65 MPa	σ_{enref}	95 MPa
σ^r_{yy}	100 MPa	f_0	0.6
σ^r_{xy}	0 MPa	d_c	.05 mm
a	0.011	v_0	10e − 6 m/s
b	0.014	φ_{Edil1}	0.0°
G	10 GPa	φ_{Edil2}	0.0°
v_p	0.1	φ_{edil2}	1°
E_0	1 mm	φ_{edil2}	0.1°
e_0	.01 mm	P_{inj}	58 MPa
E_{res}	.002 mm	T_{inj}	200°C
e_{res}	.0002 mm	b_w	100 m
η	20 MPa/(m/s)		

a constant rate, defined as P'_{inj}. A variety of rates were used. In 14 of the simulations, Cases B1–B14, the injection pressure was kept constant if it dropped to 51 MPa. In 13 simulations, Cases C1–C13, the injection pressure was kept constant if it dropped to 53 MPa. In some of the cases, the minimum injection pressure was not reached before injection was stopped.

Three additional simulations were performed (Cases D1–D3). All used constant pressure injection at 58 MPa, like Case A8. D1 tested the effect of void aperture dilation with slip by using a value of φ_{Edil} equal to 1°, instead of the baseline value of 0° (no void dilation with slip). D2 used d_c equal to 5 mm, 100 times larger than the baseline value. D3 produced fluid at 3.0 l/s after the end of injection.

Table 3 specifies the settings for all the simulation runs. Table 4 provides the values for P'_{inj} used in Cases B1–B14 and Cases C1–C13. Unless listed in Table 3, all parameters are the same as the baseline parameters given in Table 2.

Table 3. Parameters of the various simulation cases, A1–A8, B1–B14, C1–C13, and D1–D3. Further details about the B and C cases are given in Table 4.

A1–A8	Constant P_{inj} from 51 MPa to 58 MPa at 1 MPa increments
B1–B14	Decreasing P_{inj} with time from 58 MPa, minimum $P_{inj} = 51$ MPa
C1–C13	Decreasing P_{inj} with time from 58 MPa, minimum $P_{inj} = 53$ MPa
D1	Constant P_{inj} at 58 MPa, $\varphi_{Edil1} = 1.0°$
D2	Constant P_{inj} at 58 MPa, $d_c = 5$ mm
D3	Constant P_{inj} at 58 MPa, production at 3.0 kg/s after injection

Table 4. The rate of decrease in injection pressure, P'_{inj}, for cases B1–B14 and C1–C13.

Case	P'_{inj} (MPa/hr)	Case	P'_{inj} (MPa/hr)
B1	−Infinity	C1	−Infinity
B2	−10.1	C2	−7.2
B3	−5.0	C3	−3.6
B4	−3.4	C4	−2.4
B5	−2.5	C5	−1.8
B6	−2.0	C6	−1.4
B7	−1.7	C7	−1.2
B8	−1.4	C8	−1.0
B9	−1.3	C9	−0.9
B10	−1.0	C10	−0.7
B11	−0.8	C11	−0.6
B12	−0.6	C12	−0.5
B13	−0.5	C13	−0.4
B14	−0.4		

RESULTS

Plots of injection rate, injection pressure, and event magnitude versus time for Cases A3, A6, A8, B6, B10, D1, D2, and D3 are shown in Figures 2, 3, 4, 5, 6, 7, 8, and 9. Figures 10, 11, and 12 give summary metrics for Cases A1–A8. Figure 10 shows

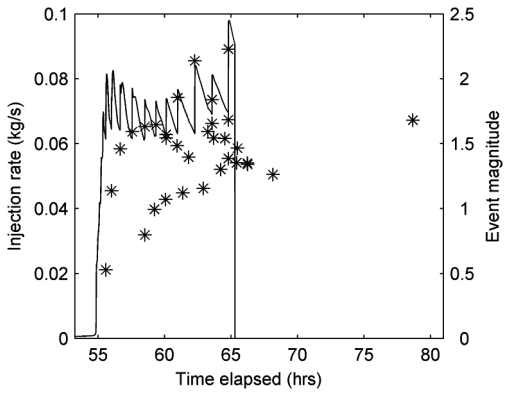

Figure 2. Injection rate (kg/s) and event magnitude for Case A3, constant pressure injection of 53 MPa.

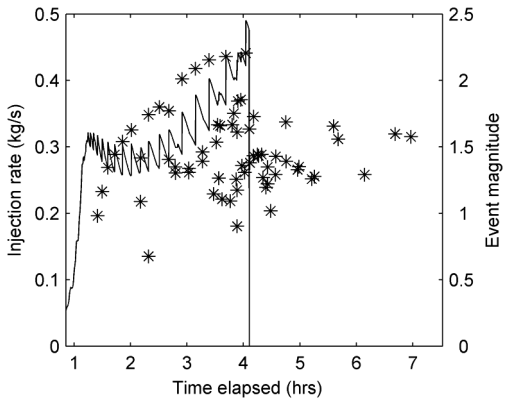

Figure 3. Injection rate (kg/s) and event magnitude for Case A6, constant pressure injection of 56 MPa.

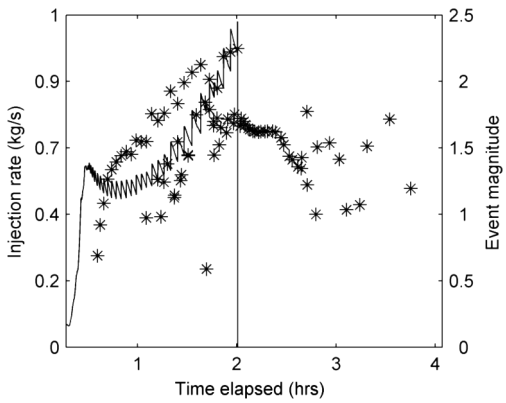

Figure 4. Injection rate (kg/s) and event magnitude for Case A8, constant pressure injection of 58 MPa.

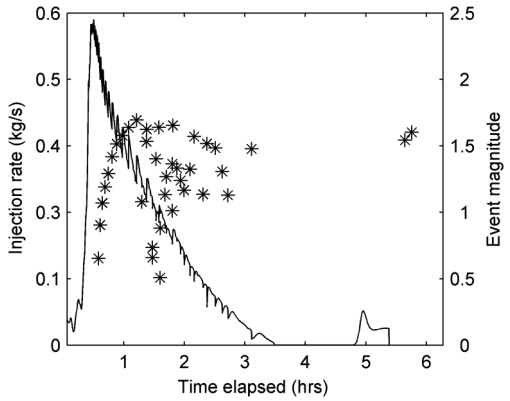

Figure 5. Injection rate (kg/s) and event magnitude for Case B6, decreasing injection rate from 58 MPa to 51 MPa with p'_{inj} equal to 2 MPa/hr.

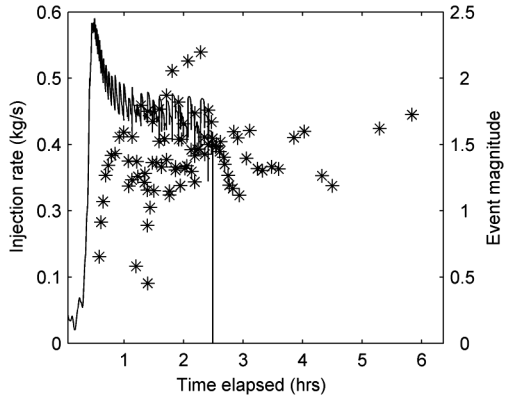

Figure 6. Injection rate (kg/s) and event magnitude for Case B10, decreasing injection rate from 58 MPa to 51 MPa with p'_{inj} equal to 1 MPa/hr. Note that in this case the injection was stopped before p_{inj} reached 51 MPa.

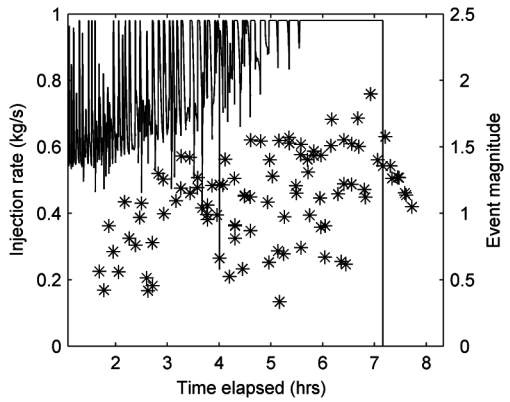

Figure 7. Injection rate (kg/s) and event magnitude for Case D1, constant pressure injection of 58 MPa with shear-induced pore volume dilation.

maximum magnitude and number of seismic events magnitude greater than two. Figure 11 shows the average injection rate during the period of time between the first seismic event and shut-in. Figure 12 shows the total fluid injected and total seismic moment released. Figures 13 and 14 show the maximum event magnitude and the number of events magnitude greater than two for Cases

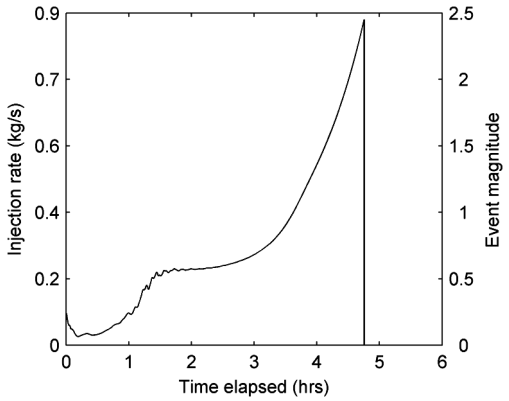

Figure 8. Injection rate (kg/s) and event magnitude for Case D2, constant pressure injection of 58 MPa with d_c equal to 5 mm, 100 times larger than the default.

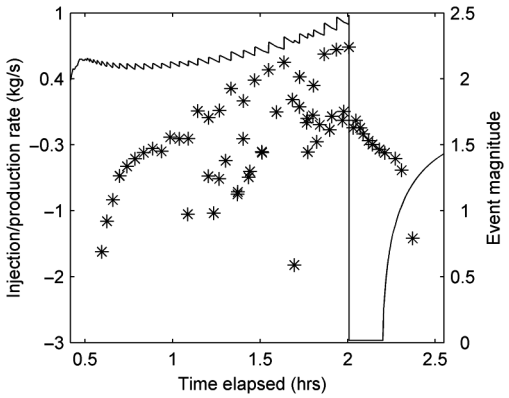

Figure 9. Injection rate (kg/s) and event magnitude for Case D3, constant pressure injection of 58 MPa with fluid production after injection.

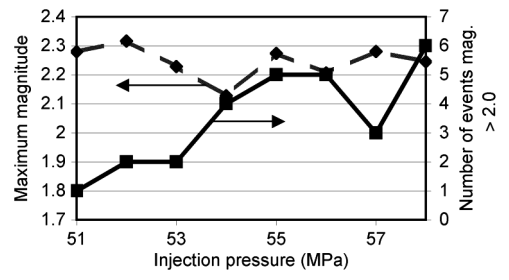

Figure 10. Maximum magnitude and the number of events with magnitude greater than 2.0 for Cases A1–A8, constant pressure injection.

B1–B14 and Cases C1–C13. Tables 5 and 6 give summary data for selected cases.

DISCUSSION

A number of issues are discussed in the following subsections. First the overall behavior of the model is discussed, focusing on comparison to EGS field observations, the sequential stimulation mechanism that controlled the progression of the stimulation, shut-in events, and changes in injection rate with time. Subsequent subsections discuss estimation of least principal stress, estimation of prestimulation hydraulic diffusivity, the effect of injection pressure for constant pressure injection, the effect of changing injection pressure with time, the effect of producing back fluid to reduce shut-in seismicity, a comparison of rate and state to static/dynamic friction, the effect of slip-induced void aperture dilation, and the effect of the characteristic displacement scale, d_c.

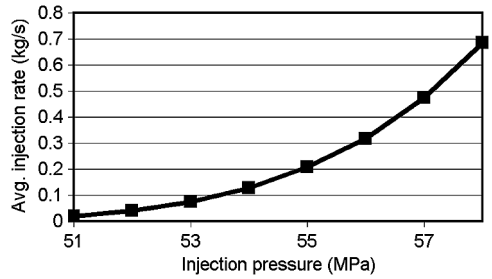

Figure 11. Average injection rate during stimulation for Cases A1–A8, constant pressure injection.

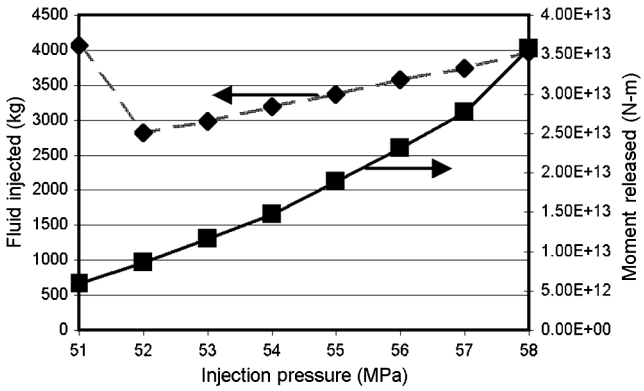

Figure 12. Total fluid injected (kg) and total seismic moment release (N-m) for Cases A1–A8, constant pressure injection.

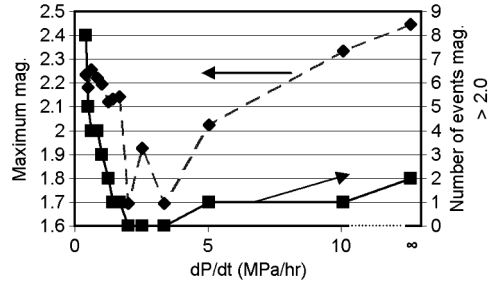

Figure 13. Maximum magnitude and the number of events with magnitude greater than 2.0 for Cases B1–B14, decreasing injection pressure with time from 58 MPa to a minimum of 51 MPa.

Similarity and differences compared to EGS field observations

The behavior of the model was qualitatively consistent with a broad range of observations from EGS projects, with some differences. Similarities were migration of event hypocenters away from the stimulated region (Figure 15; Baisch et al., 2010; Shapiro et al., 1999), shut-in seismicity after injection stopped (Figures 2, 3, 4, 5, 6, 7, 8, and 9; Charléty et al., 2007; Häring et al., 2007; Asanuma et al., 2006; Baisch et al., 2010), and large increases in injection pressure with small changes in injection rate (Figure 11; Cornet et al., 2003). Differences were an underestimation of the number of smaller events (Figures 2, 3, 4, 5, 6, 7, 8, and 9; Baisch et al., 2010), a lack of event hypocenters that were *not* at the periphery of the stimulated region (Figure 15; Baisch et al., 2010), and shut-in seismicity magnitudes that were lower than magnitudes

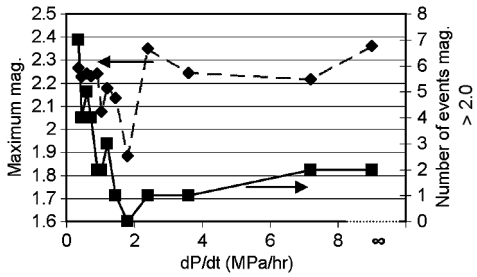

Figure 14. Maximum magnitude and the number of events with magnitude greater than 2.0 for Cases C1–C13, decreasing injection pressure with time from 58 MPa to a minimum of 53 MPa.

Table 5. Summary data for Cases A1, A3, A6, A8, B6, B10, and D1–D3. The number of events magnitude greater than 2.0, the maximum magnitude during injection, the maximum magnitude after injection, the total number of events during injection, and the total number of events after injection.

Case	Events >2.0	Max. mag. during injection	Max. mag. after injection	Events during injection	Events after injection
A1	1	2.3	—	7	0
A3	2	2.2	1.7	26	6
A6	5	2.2	1.7	41	25
A8	6	2.2	1.8	51	32
B6	0	1.7	1.6	35	2
B10	3	2.2	1.7	61	24
D1	0	1.9	1.4	88	8
D2	0	—	—	0	0
D3	6	2.2	1.7	51	11

during injection (Figures 2, 3, 4, 5, 6, 7, 8, and 9; Asanuma et al., 2006; Baisch et al., 2010; Majer et al., 2007). Because an unrealistically low value of storativity was used, it was necessary to keep the injection rate low by using a low value of permeability, as discussed in Appendix B.

The differences between the model behavior and reality probably occurred because the model was significantly less heterogeneous than a natural system. The model contained a single, linear fracture with homogenous properties (other than permeability). Actual EGS stimulations could involves several fracture zones with multiple slip surfaces, nonuniform properties, and nonplanar geometry. All of these factors would encourage heterogeneity in the location of hypocenters and a greater number of smaller events.

As discussed in the section "Effect of shear-induced pore volume dilation," shear-induced pore volume dilation could also cause hypocenters that are not located at the periphery of the stimulated region, especially because fractures in EGS stimulations are often embedded in high porosity damaged zones. As discussed in the section "Effect of d_c," d_c controls the minimum seismic event magnitude (Ruina, 1983; Dieterich, 2007). If a smaller value of d_c had been used, smaller events could have been simulated. In that case, it would have been necessary to use a finer discretization to avoid numerical instability (Lapusta, 2001). As discussed in the section "Shut-in seismicity," the shut-in events had lower magnitude likely because the fracture modeled was 1D, not 2D.

In rate and state simulations with appropriately refined discretizations and homogenous (or mostly homogenous) properties on a single fracture, frequency-size distributions tend toward a "characteristic" distribution (Rice, 1993). In such models, seismic events, once nucleated, have a tendency to propagate across the entire fracture. In contrast, "inherently discrete" models have coarser discretizations and often use less realistic friction laws and tend to reproduce Gutenberg-Richter frequency-size distributions that have a much greater number of smaller events than larger events (Rice, 1993; Ben-Zion and Rice, 1993; Ben-Zion, 2008). The development of characteristic frequency-size distributions in rate and state simulations suggests that Gutenberg-Richter distributions are not necessarily a consequence of frictional behavior, but rather may arise from heterogeneity in the earth itself. Hillers et al. (2006) replicated a Gutenberg-Richter distribution on a single fault using a rate and state model with spatial heterogeneity in frictional parameters. Aftershock distributions have been modeled successfully with rate and state friction using a distribution of faults (Gomberg et al., 2005).

Sequential stimulation mechanism

The advance of the stimulated region occurred through a specific mechanism, which we refer to as the sequential stimulation (SS) mechanism. A similar mechanism was described in McClure and Horne (2010) based on results from a simpler shear stimulation model.

Conceptually, it is useful to divide the fracture into two regions. In the stimulated region, significant slip had already occurred. The permeability had increased dramatically, and as a result the fluid pressure had increased significantly. In the unstimulated region, slip had not yet occurred. The permeability was low, and the fluid pressure was near the initial pressure because fluid had not had time to flow beyond the stimulated region. Figures 16, 17, and 18 show the pressure distribution in the fracture at various times during Cases A8, A4, and A1.

Slip events tended to nucleate at the edge of the stimulated region. Once nucleated, slip could propagate easily back across the stimulated region because in the stimulated region the fluid pressure was high and friction was relatively weak. It was more difficult for slip to propagate from the stimulated region into the unstimulated region because in the unstimulated region fluid pressure remained low and friction was relatively strong. Nevertheless, slip events were able to propagate some distance into the unstimulated region before stopping. When that happened, the permeability increased rapidly on the patch of fracture that had slipped for the first time. Fluid was able to rush into the newly slipped patch of fracture, weakening friction and nucleating the next seismic event.

Figures 2, 3, and 4 show that for the base case with constant injection pressure, seismic events were relatively low in magnitude at the beginning of injection and grew larger over time. Magnitude increased over time because magnitude is related directly to the surface area of fracture that slips. At later times, more fracture was available to slip. A similar effect was observed in numerical simulations by McClure and Horne (2010) and by Baisch et al. (2010).

Table 6. Summary data for Cases A1, A3, A6, A8, B6, B10, and D1–D3. The total seismic moment release both during and after injection, the total duration of injection (including the period prior to the first seismic event), the total amount of fluid injected, and the maximum shear displacement along the fracture.

Case	Moment during inj. (N-m)	Moment after inj. (N-m)	Duration of injection (s)	Fluid injected (kg)	Maximum displacement (m)
A1	5.90E+12	0.00E+00	42,629,200	4073	0.04
A3	1.06E+13	9.66E+11	235,008	2982	0.07
A6	1.87E+13	4.44E+12	14,759	3585	0.11
A8	2.75E+13	8.26E+12	7227	3981	0.14
B6	5.52E+12	3.15E+11	19,374	2633	0.06
B10	1.81E+13	4.31E+12	8953	3622	0.11
D1	9.24E+12	6.08E+11	25,781	20,538	0.12
D2	0.00E+00	0.00E+00	17,113	4752	0.15
D3	2.74E+13	2.19E+12	7227	3981	0.14

Shut-in events

Shut-in events occurred because of pressure redistribution. During injection, there was a pressure gradient away from the wellbore, which can be seen in Figures 16, 17, and 18. After injection stopped, the pressure redistributed to become uniform everywhere. The redistribution lowered pressure near the injector and increased pressure away from the injector. The fluid pressure at different times following shut-in during Case A8 is shown in Figure 19.

The idea that pressure diffusion could cause an advance of the pressure front after shut-in has been proposed by other authors. Healy et al. (1968) and Hsieh and Bredehoeft (1981) discussed the possibility that this may have occurred in association with a deep wastewater disposal well outside of Denver. Several numerical models have predicted this effect, including Bruel and Charlety (2007), McClure and Horne (2010), Baisch et al. (2010), and Baisch et al. (2006). Similar mechanisms were investigated in modeling by Hayashi and Abe (1982) and Hayashi and Abe (1983).

The shut-in events were smaller in magnitude than the largest events during injection. In actual EGS stimulation, shut-in events are often larger than events during injection (Majer et al., 2007).

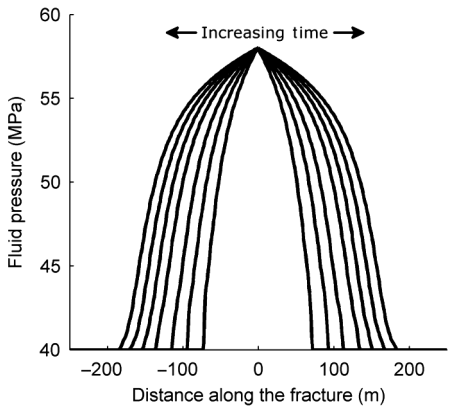

Figure 15. The distance of each seismic event hypocenter from the injector well as a function of duration of injection for Case A8, constant pressure injection at 58 MPa.

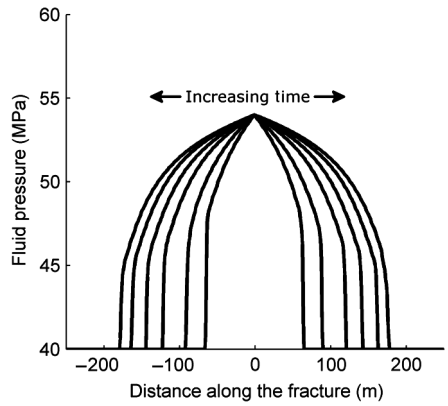

Figure 16. Pressure distribution along the fracture at various times during stimulation for Case A8, constant pressure injection at 58 MPa. The injector is located at the middle. The pressure front moves outward with time.

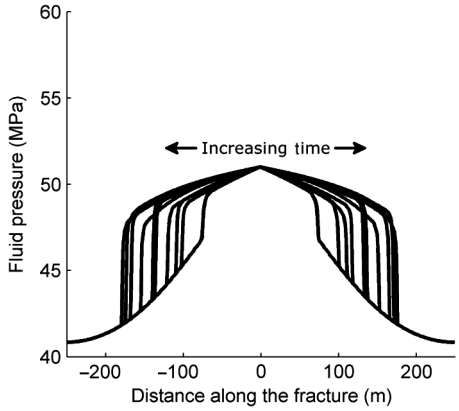

Figure 17. Pressure distribution along the fracture at various times during stimulation for Case A4, constant pressure injection at 54 MPa. The injector is located at the middle. The pressure front moves outward with time.

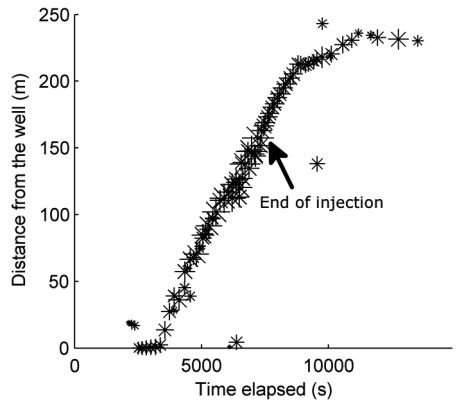

Figure 18. Pressure distribution along the fracture at various times during stimulation for Case A1, constant pressure injection at 51 MPa. The injector is located at the middle. The pressure front moves outward with time.

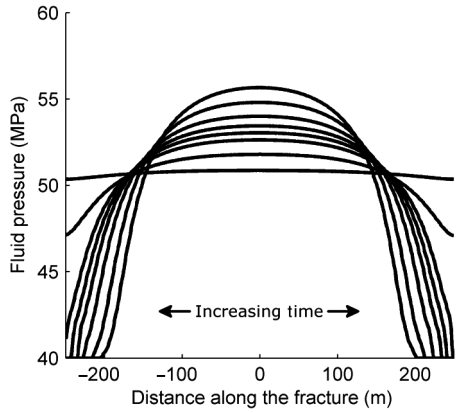

Figure 19. Pressure distribution along the fracture at various times during shut-in following injection for Case A8, constant pressure injection at 58 MPa. The injector is located at the middle. The pressure front flattens out with time.

The discrepancy may be partly an artifact of our use of a 1D fracture. For a 2D planar fracture, the periphery would have relatively more surface area than in the 1D case. The shut-in events, which occur at the periphery, would be relatively larger.

In the 1D simulations, peripheral events on either side of the fracture tended to be separated because the center region, which did not slip, prevented slip on one side from triggering slip on the other. For a 2D, planar fracture, the periphery would be a ring-shaped region, and there would be no barrier to prevent slip anywhere in the periphery from inducing slip everywhere else in the periphery. Baisch et al. (2010) simulated induced seismicity in a 2D planar fracture and observed larger events during shut-in than during injection.

Changes in flow rate with time

The flow rate behavior with time for several cases can be seen in Figures 2, 3, 4, 5, 6, 7, 8, and 9. The flow rate tended to spike following a seismic event. Seismic events caused abrupt increases in permeability along the fracture without changing the pressure distribution (except in Case D1, which included the effect of shear-induced pore volume dilation). Because flow rate is proportional to permeability and pressure gradient, increasing permeability while holding pressure gradient constant increased flow rate. Between seismic events, flow rate tended to decrease, as would be expected for constant injection pressure.

During an actual EGS stimulation, it is typical for flow rate to be held constant (except for occasional step changes) and the injection pressure to fluctuate with time. Abrupt changes in injection pressure of at least 0.6 MPa following large slip events have been observed during actual EGS stimulations (Weidler, 2000). The magnitude of the changes in injection pressure observed during EGS stimulations do not appear to be as great as the fluctuations in flow rate observed in Figures 2, 3, 4, 5, 6, 7, 8, and 9. However, as discussed in the following section, "Implications of the sequential stimulation mechanism for estimation of least principal stress," small changes in injection pressure can cause large changes in flow rate during shear stimulation. It follows that changes in fracture permeability would cause relatively small changes in injection pressure for constant injection rate and relatively large change in injection rate for constant injection pressure.

Outside of short term fluctuations, the long-term behavior of the injection rate was generally increasing with time for most of the constant pressure injections, but sometimes decreased or remained constant with time. The relationship between flow rate and injection pressure involved competing effects, and can be understood through the framework of the SS mechanism. Increasing permeability across the stimulated region tended to cause an increase in injection rate with time. Growth of the stimulated region tended to cause a decrease in injection rate with time. A more detailed discussion of this relationship can be found in McClure and Horne (2010).

Implications of the sequential stimulation mechanism for estimation of unstimulated hydraulic diffusivity

It is sometimes assumed that the advance of the seismicity cloud during shear stimulation is caused by diffusion of pressure into the unstimulated reservoir (Shapiro et al., 1999; Bruel, 2007; Shapiro and Dinske, 2009). This process has been modeled assuming that the permeability is constant (Shapiro et al., 1999) or that permeability increases with fluid pressure (Shapiro and Dinske, 2009). The migration of event hypocenters from the injector has been used to estimate the unstimulated hydraulic diffusivity of the formation (Shapiro et al., 1999; Bruel, 2007). This method of estimating the unstimulated hydraulic diffusivity depends on the assumption that pressure diffuses through the unstimulated fractures ahead of the permeability stimulation front.

In the SS mechanism, friction weakening allows slip and permeability enhancement to advance ahead of the pressure front. The growth of the stimulated region depends on the stimulated diffusivity and has no dependence on the unstimulated diffusivity (McClure and Horne, 2010). In practice, which process can advance faster would depend on the relative hydraulic diffusivities of the stimulated and unstimulated fractures, the frictional characteristics of the fractures, the geometry of the fractures, and the initial stress state.

The initial hydraulic diffusivity could not be estimated from the growth of the seismic cloud if the stimulation front were able to advance faster than pressure can diffuse through the unstimulated region.

Implications of the sequential stimulation mechanism for estimation of the least principal stress

It was proposed by Cornet and Bérard (2003) and subsequently assumed in Cornet et al. (2007) and Valley and Evans (2007) that during the hydraulic stimulation of the wells GPK1, GPK3, and GPK4 as a part of the EGS projects at Soultz, France, the fluid pressure reached the least principal stress at the top of the openhole section during stimulation. That assumption was used to estimate the magnitude of the least principal stress at Soultz field.

The justification for this assumption was that during the stimulation, large increases in injection rate resulted in relatively small increases in injection pressure. This behavior could be referred to as pressure limiting behavior. When pressure limiting behavior occurs during hydraulic stimulation involving the growth of tensile cracks, it is taken as evidence that tensile fractures are propagating away from the wellbore (Zoback, 2007).

Our model suggests that shear stimulation alone, without the presence of tensile fracturing, could cause pressure limiting behavior. Figure 11 shows the average flow rate for different constant injection pressures during stimulation between the first seismic event and shut-in. It is evident that for the lowest injection pressure case, 51 MPa in Case A1, the average flow rate was extremely low. For an even lower injection pressure, the fluid pressure would not be high enough to propagate slip regardless of the duration of injection. That pressure could be called the shear stimulation threshold pressure.

For injection pressures below the shear stimulation threshold, increasing injection rate in increments would result in relatively large increases in injection pressure because injectivity would be related to the initial, low permeability.

Once shear stimulation began to occur, further increases in injection rate would result in much lower increases in injection pressure. From Figure 11, during Case A1 (51 MPa downhole, corresponding to a $\Delta P = P_{inj} - P_{init}$ of 11 MPa), the average flow rate (during the period between the first seismic event and shut-in) was 0.02 kg/s. Increasing the injection pressure by one additional mega-Pascal to 52 MPa in Case A2 (ΔP of 12 MPa, an increase of 9% from Case A1), doubled the flow rate to 0.04 kg/s. In Case A8, with an injection pressure of 58 MPa, the average flow rate was about

0.7 kg/s. From Case A1 to Case A8, a 64% increase in ΔP resulted in an increase in injection rate of 3400%.

The large increases in injection rate can be explained by considering the pressure distribution at different times during injection. The difference between the initial fluid pressure and the injection pressure can conceptually be decomposed into two parts. One part is the pressure drop in the stimulated region from the wellbore to the edge of the stimulated region. The second part is the front extension pressure at which the stimulated region was able to advance. The front extension pressure is approximately the fluid pressure that must be reached at the edge of the stimulated region to trigger seismicity that spreads slip into the unstimulated region. At the edge of the stimulated region, the fluid pressure drops rapidly from the front extension pressure to the initial fluid pressure.

Increasing the injection pressure lowered the front extension pressure. In Figure 18, injection at 51 MPa, the extension pressure was around 48 MPa. In Figure 17, injection at 55 MPa, the extension pressure was around 44 MPa. In Figure 16, injection at 58 MPa, the extension pressure apparently had reached nearly 40 MPa, the initial fluid pressure.

The pressure gradient was roughly the difference between the injection pressure and the front extension pressure divided by the distance to the fracture tip. Increasing injection pressure increased pressure gradient in two ways: increasing the pressure at the center of the stimulated region and decreasing it at the edge (by lowering the extension pressure). Further discussion of the relationship between injection pressure and rate can be found in McClure and Horne (2010).

From equation 13, higher fluid pressure led to higher permeability. In addition, greater displacement occurred with higher injection pressure, which also led to greater permeability.

Therefore, when the SS mechanism controlled stimulation, small increases in injection pressure led to large increases in injection rate.

If injection pressure were less than the shear stimulation threshold, significant slip would not occur, and permeability would remain low. With low permeability, the injection rate would remain low, and increases in injection pressure would cause small increases in injection rate.

Therefore, there are different mechanisms controlling the relationship between injection pressure and injection rate for injection pressures above and below the shear stimulation threshold. Injection rates at pressures below the stimulation threshold are related to the initial permeability. Injection rates at pressures above the stimulation threshold are related to the SS mechanism and depend on the much higher stimulated permeability. The change in mechanism at the stimulation threshold causes a sharp change in the relationship between injection pressure and rate.

The shear stimulation threshold pressure could be significantly below the least principal stress. In our model, it was roughly 50 MPa, 15 MPa less than the least principal stress.

Our modeling suggests that pressure limited behavior could occur because of shear stimulation. If pressure limited behavior were incorrectly taken to be evidence of tensile fracturing, the least principal stress could be underestimated.

Effect of injection pressure for constant pressure injection

Cases A1–A8 investigated the effect of injection pressure for constant pressure injection. Plots of flow rate and event magnitude with time for Cases A3, A6, and A8 are shown in Figures 2, 3, and 4.

The maximum event magnitude was not affected significantly by the injection pressure. Figure 10 shows that maximum magnitudes were clustered around 2.25 for all cases. The highest magnitudes occurred in Cases A1 and A2, the lowest injection pressures. They were larger because in those cases injection went on for a very long time before the first seismic event occurred (Figure 20). As a result, the pressure in the unstimulated region was significantly elevated by the time seismicity began (Figure 18).

The maximum event magnitude was generally not affected by injection pressure because the stress drop during an earthquake is weakly sensitive to the fluid pressure. Magnitude is related to the product of the area of slip and the displacement. Displacement is related to the stress drop and area of slip. The maximum area of slip was roughly the same in each simulation because it was limited by the size of the fracture. The stress drop is related to the weakening of friction caused by a decrease in the θ variable in the rate and state friction law. The decrease in θ during an earthquake depends on the rate and state parameters such as a, b, and η, but not on the effective normal stress.

Higher injection pressure led to a greater release of seismic moment, a somewhat greater amount of total fluid injected, and a greater number of relatively large events. These effects can be seen in Figures 10 and 12. The higher injection pressure caused a greater weakening of friction, which allowed more slip to occur, a greater release of seismic moment and more relatively large events.

Effect of decreasing injection pressure over time

Cases B1–B14 and Cases C1–C13 tested the effect of decreasing the injection pressure over time. Plots of flow rate and event magnitude with time for Cases B6 and B10 are shown in Figures 5 and 6. In all cases, the initial injection pressure was 58 MPa. The injection pressure was kept constant at 58 MPa until the first seismic event, and then it began to be decreased. In the different cases, the pressure was decreased at different rates with respect to time. In Cases B1–B14, injection pressure was kept constant once it reached 51 MPa. In Cases C1–C13, injection pressure was kept constant once it reached 53 MPa. The cases varied from instantaneous drop to the minimum injection pressure (Cases B1 and C1) to constant injection pressure at 58 MPa (Cases B14 and C13, the same as Case A8). It should be apparent that there was some overlap between Cases B1–B14 and Cases C1–C13.

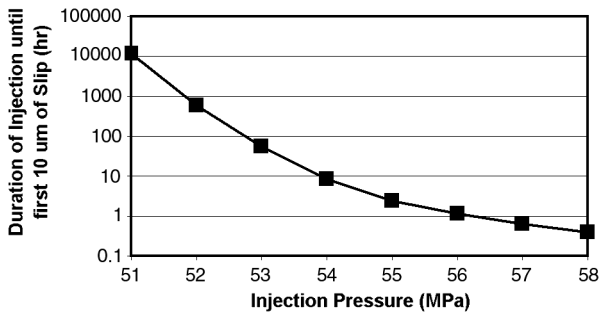

Figure 20. The duration of time until maximum slipping velocity on the fracture reached 10 μm/s for Cases A1–A8, constant pressure injection.

Figures 10, 13, and 14 show that the cases with decreasing injection pressure over time had reduced seismicity compared to any of the constant injection pressure cases. There was a range of optimal values for p'_{inj}, the pressure derivative, that resulted in significantly smaller maximum magnitudes and fewer events magnitude greater than 2.0 than for either constant injection at 51 MPa, 53 MPa, or 58 MPa. The effect was more pronounced for Cases B1–B14 than Cases C1–C13.

There is a physical explanation for why decreasing injection pressure with time reduced seismicity. Magnitude is related to slip area and shear displacement. The largest events were able to propagate across the entire stimulated region, with the largest events occurring when the stimulated region was largest.

Decreasing the injection pressure over time tended to decrease the fluid pressure across the entire stimulated region over time. Because friction strengthens as pressure decreases, this had the effect of gradually strengthening friction across the fracture over time. Events continued to nucleate at the edge of the stimulated region, but they faced greater frictional resistance in spreading back across the stimulated region. This caused fewer events to spread across the entire stimulated region, and when they did, their total displacements were smaller.

The optimal values of p'_{inj} corresponded to cases where the minimum injection pressure was reached either some time before or around the time that injection was complete. If injection pressure was lowered too rapidly, the minimum injection pressure was reached early in the stimulation, and the stimulation was subsequently carried out as a constant pressure injection. If injection pressure was lowered too slowly, the magnitude damping effect of lowering injection pressure over time was limited.

The effect of decreasing injection pressure over time was more pronounced for Cases B1–B14 than C1–C13. In Cases B1–B14, the minimum injection pressure was 51 MPa. Interestingly, in Case A1, 51 MPa injection was almost too low to cause stimulation. Figure 20 shows that for Case A1 it took an exceptionally long time, over 1000 hours of injection, for slip velocity to reach 10^{-5} m/s. Prior to the initiation of significant slip, Case A1 was effectively constant pressure injection into a low permeability fracture. In Cases B1–B14, injection at 51 MPa was clearly able to propagate stimulation across the fracture. It appears that a higher injection pressure was required to initiate seismicity in Case A1, but once seismicity was initiated, it was possible to propagate stimulation with a lower injection pressure.

The exact value of P'_{inj} that would minimize seismicity is dependent on the details of the model. If decreasing injection pressure with time were to be attempted in practice, the optimal P'_{inj} would be site specific and need to be estimated in advance with the construction of a full scale stimulation model.

It is possible that with a more complex, site-specific model, the conclusions of this section may not hold or may not be feasible. On the other hand, with a more detailed model perhaps other opportunities to minimize induced seismicity would become apparent. Our results demonstrate in concept that minimizing induced seismicity by manipulating injection strategy could be possible, but to do so would require careful modeling and planning.

Effect of producing fluid back after injection

Case D3 tested the effect of producing fluid back after injection. Prior to the end of injection, Case D3 was identical to Case A8, with constant pressure injection at 58 MPa. The injection rate and event magnitudes for Cases A8 and D3 are shown in Figures 4 and 9 (the vertical scales are different in the two figures). The figures show that producing from the well following injection resulted in reduced postinjection seismicity. The strategy of producing back fluid was also suggested by Baisch et al. (2006).

Producing fluid back mitigated the build-up of fluid pressure at the edge of the stimulated region after shut-in. The postinjection events immediately after the end of injection were not prevented because it took a period of time for the pressure transient caused by the production to reach the periphery of the fracture.

Effect of shear-induced pore volume dilation

Case D1 investigated the potential effect of shear-induced pore volume dilation on seismicity. Laboratory experiments such as Marone et al. (1990) and Morrow and Byerlee (1989) show evidence of fracture pore volume dilation due to sliding. The effects of pore volume dilation have been investigated numerically by several authors, including Segall and Rice (1995), Yamashita (1999), and Segall et al. (2010). We are not aware of field evidence to indicate whether or not shear-induced pore volume dilation happens during EGS stimulation, but it is an interesting phenomenon to investigate.

Pore volume dilation had the effect of damping out seismicity, consistent with results from Yamashita (1999), Segall and Rice (1995), and Segall et al. (2010). This can be seen by comparing Cases D1 and A8 in Figures 7 and 4, which show event magnitude with time. Both show constant pressure injection at 58 MPa. The only difference between the two cases is that there was shear-induced pore volume dilation in Case D1. With pore volume dilation, a larger number of events occurred, but they were of relatively smaller magnitude.

Pore dilation damped out slip events because it caused a decrease in fluid pressure during slip. During rapid slip, fluid flow did not have time to occur, and so the mass of fluid at a given location was nearly fixed. Water density is relatively insensitive to pressure, so to conserve mass, the void aperture at a given location had to be nearly constant during slip. As slip tried to dilate the void aperture, the only way to keep void aperture constant was to decrease fluid pressure, increasing the effective normal traction (equation 13). The higher effective normal traction strengthened friction and tended to inhibit slip from occurring. The same total amount of slip had to occur for the same injection pressure, and so slip was distributed into a larger number of smaller magnitude events.

There were several other differences between Case D1 and the other simulations. Due to pore dilation, the fluid pressure at the injector was decreased following seismic events. Because the well continued to inject at constant pressure, the flow rate spiked as a large pressure gradient was suddenly imposed between the injector and the fracture. Unrealistically high flow rates were possible, and so it was necessary to specify a maximum injection rate of 1 kg/s in the code. Because of the maximum flow rate, the injection rate would sometimes dip below the target of 58 MPa. Because of flow rate spiking following slip events, the flow rate history had a very erratic, unrealistic looking behavior as can be seen in Figure 7.

There were more event hypocenters near the injector in Case D1 than in Case A8. After seismic events, when fluid pressure was lowered near the injector, the fluid pressure increased again rapidly near

the wellbore. Often that triggered another seismic event close to the injector.

A more realistic treatment of fracture zone geometry may have damped out the erratic variations in flow rate. If a fracture were surrounded by porous, permeable material, such as the alteration zones observed at Soultz (see Appendix B), fluid could flow rapidly back into the fracture from the surrounding porosity and raise the fluid pressure up again across the entire fracture. Such a mechanism could lead to complicated behavior that could be interesting to investigate in future work. For example, a rapid decrease in fluid pressure during slip followed by a rapid increase in pressure due to fluid flow from a surrounding damage zone could lead to aftershock sequences with hypocenters distributed throughout the stimulated region as fluid pressure rapidly recovered following slip events.

A final difference between Case D1 and the other cases was that far more fluid was injected in Case D1 (Table 6). The reason was that because of the shear-induced pore volume dilation, a greater amount of fluid was required to increase the fluid pressure across the fracture.

Effect of d_c

In Case D2, a larger value of d_c resulted in inhibited seismicity. The entire fracture was stimulated, but the slip was slow and aseismic. Figure 8 shows the injection rate and event magnitude with time for Case D2. The injection rate increased continuously during injection because of the shear-induced stimulation, but seismicity did not occur. This result is consistent with the theory of rate and state friction (Ruina, 1983), which predicts that the minimum size of a patch that can slip unstably increases with d_c. If the fracture in Case D2 had been large enough, the region of increased fluid pressure would have eventually grown large enough that it would have slipped unstably in a seismic event.

Differences in the rate and state parameters a, b, and d_c in nature help explain why sometimes fractures slip seismically, and sometimes they slip aseismically. Before initiating an injection experiment at a given location, characterization of the parameters a, b, and d_c could be useful for predicting seismic hazard.

Comparison of rate/state friction to static/dynamic friction

Previously, in McClure and Horne (2010), we modeled injection into a 1D, isolated fracture using static/dynamic friction instead of rate and state friction. See Appendix A for a description of static/dynamic friction. The problem setup was similar, but not identical, to the problem setup used in this paper. An approach similar to that used in McClure and Horne (2010) was used by Baisch et al. (2010), who modeled injection-induced seismicity in a 2D planar fault. Many results from McClure and Horne (2010) and Baisch et al (2010) were consistent with the results from the rate and state modeling described in this paper. In all three investigations, event magnitudes increased with time as the stimulated region grew larger. Hypocenters migrated away from the injector well. Postinjection events occurred because of redistribution of pressure. Investigation of the effect of injection schedule in McClure and Horne (2010) were consistent with the results in this paper. Decreasing injection pressure over time reduced seismicity relative to other strategies. Producing fluid after injection resulted in reduced seismicity.

A difference between the rate and state simulations in this work and the results from Baisch et al. (2010) and McClure and Horne (2010) is that there were fewer low magnitude events in the rate and state simulations. The models in Baisch et al. (2010) and McClure and Horne (2010) are examples of "inherently discrete" models (Ben-Zion and Rice, 1993), which tend to model a greater number of smaller events.

CONCLUSIONS

Our modeling suggests that the treatment of friction and stress interaction between elements have a first-order effect on the overall behavior of a shear stimulation model.

The sequential stimulation mechanism was proposed to describe the process by which shear stimulation occurs in fractures and fault zones. The shear stimulation mechanism contrasts with the diffusion controlled mechanism because it involves slip and permeability enhancement advancing ahead of pore pressure perturbation.

If the sequential stimulation mechanism describes shear stimulation realistically, it would undermine assumptions that are sometimes made for the estimation of initial hydraulic diffusivity and the estimation of least principal stress.

Shut-in seismic events occurred because of redistribution of pressure after injection was stopped, a mechanism proposed by several previous investigators. Producing fluid back after injection reduced postinjection seismicity.

Reducing injection strategy over time was identified as a strategy that minimized maximum event magnitude. This result shows in principle that it may be possible to reduce the magnitude of induced events with injection strategy.

The effect of two geological factors, slip-induced pore volume dilation and the characteristic length scale in the rate and state law, were investigated. Pore volume dilation caused more smaller events and a larger characteristic length scale led to aseismic slip.

ACKNOWLEDGMENTS

We gratefully acknowledge the Precourt Institute for Energy at Stanford University for funding this research. This work has benefitted greatly from interactions with a number of people at Stanford. Thank you very much to Andrew Bradley for his insight into fast boundary element solutions, as well as the coupling of rate and state and fluid flow simulation. Thank you to Eric Dunham for his help and for lending us a rate and state simulation code which we used to check the accuracy of our simulator. Also thank you to David Pollard, Paul Segall, Mark Zoback, and Hamdi Tchelpi for providing valuable insight.

APPENDIX A

SEISMICITY MODELING IN EGS

EGS modeling most often has used a treatment of friction in which elements do not slip until their shear traction exceeds their frictional ability to resist slip according to the Coulomb failure criterion

$$|\tau| = S_0 + \mu(\sigma_n - P) \tag{A-1}$$

where τ is shear traction, S_0 is a cohesion factor, μ is the coefficient of friction, σ_n is the normal traction, and P is the fluid pressure.

If μ is assumed constant (Kohl and Mégel, 2007; Ghassemi and Tarasovs, 2006), then slip is gradual and essentially aseismic because the only friction weakening mechanism is pore pressure diffusion.

Some recent modeling has implemented methods for abruptly weakening friction on slipping elements, as occurs in earthquakes. Bruel (2007) used a constant μ, but allowed S_0 to disappear when an element reached the slipping criterion. Baisch et al. (2010) imposed an instantaneous drop in stress on slipping elements. McClure and Horne (2010) imposed an instantaneous (but subsequently recovered) drop in μ on slipping elements. In these approaches, slip occurs instantaneously and so is essentially seismic. We refer to the approach in McClure and Horne (2010) as static/dynamic friction. All of these models are more generally in the class of inherently discrete earthquake models (Ben-Zion and Rice, 1993).

Rate and state friction has several advantages compared to other approaches. Constant friction approaches can model only aseismic slip, and abruptly weakening friction can only model seismic slip. Rate and state friction can model either seismic or aseismic clip. Rate and state friction simulation allows time to be discretized during slip, allowing slip velocity to evolve continuously, although potentially very rapidly.

A variety of approaches to stress transfer have been used in EGS modeling, including the block-spring model (Baisch et al., 2010), the distinct element model (Deng et al., 2011; Rachez and Gentier, 2010), the displacement discontinuity method (Ghassemi and Tarasovs, 2006) and neglecting stress transfer (Bruel, 2007; Kohl and Mégel, 2007). The model in this paper calculated stress transfer using the displacement discontinuity method (Crouch and Starfield, 1983). The displacement discontinuity method assumes linearly elastic deformation in an infinite, isotropic, homogenous medium.

APPENDIX B

RELATIONSHIP OF OUR MODEL TO ACTUAL EGS RESERVOIRS

Observations made during EGS projects demonstrate the context of this work. The European EGS project at Soultz-sous-Forêts can be used as an example of an EGS project. During the 1990s and 2000s several wells were drilled and stimulated hydraulically in faulted and fractured granite. During each stimulation, thousands of cubic meters of water were injected at high pressure into open wellbore. The injectivity of the wells increased by one to two orders of magnitude following stimulation (Hettkamp et al., 2004; Tischner et al., 2006; Genter et al., 2010).

Spinner and temperature logs of the Soultz wells indicated that during hydraulic stimulation, fluid exited the wellbore at a small number of preexisting fracture zones intersecting the wellbore. Caliper and wellbore imaging logs indicated that the newly permeable fractures had existed prior to stimulation but had been induced to shear, enhancing their permeability. In one example, 70% of flow during injection exited the wellbore GPK3 at a single location. (Evans et al., 2005a; Evans et al., 2005b; Baria et al., 2006; Tischner et al., 2006; Dezayes et al., 2010).

Wellbore core demonstrated that a typical fracture zone consisted of a fault core surrounded by an alteration zone up to 25 m thick. The fault cores were full of cataclasites, breccia, and secondary precipitation of quartz. The alterations zones had high fracture density and extensive chemical alteration leading to porosities as high as 25% (Genter et al., 2000).

The fault zones observed at Soultz could be considered more or less typical for medium to large-scale faults in granite (Wibberley et al., 2008; Caine et al., 1996; Bruhn et al., 1994; Lockner et al., 2009). However, other fault zones geometries in granite have been described in the literature (Griffith et al., 2009).

In this work, injection into a single, isolated fracture 500 m long was modeled. While there may be a large number of fractures participating in flow at Soultz, they are located primarily in a small number of large scale fracture zones. The larger seismic events require a laterally extensive slip surface (Charlety et al., 2007) and so are likely associated with the fault core. The fracture in our model is intended to represent the fault core. Such a model cannot describe all of the smaller scale seismic events that occur on minor fractures, but it can describe slip on the large scale features.

One challenge for EGS modeling is how to specify the model storativity. Closed fractures in granite (which would be any fracture in frictional contact, and therefore capable of generating an earthquake) have apertures on the order of hundreds of microns (Esaki et al., 1999; Lee and Cho, 2002). A huge number of such fractures would be required to contain the thousands of cubic meters that are injected during EGS stimulation. Because fluid typically exited the wellbore from a small number of fracture zones, a likely source of storativity is the high porosity, heavily fractured alteration zones that surround the fault cores.

In this work, we avoided any complexity associated with the details of fracture zone geometry. We modeled flow only in a single fracture. The storativity of the fracture was supplied by the increase in void aperture caused by increase in fluid pressure, which resulted in a decrease in effective normal stress (equation 13. Void aperture values were on the order of 10^{-3} m, and so the fracture had quite limited volume and storativity.

Because the fracture storativity was low, it was necessary to use low flow rates, generally around 1 kg/s. During actual stimulations at Soultz, injection rates reached 50 kg/s or higher (Tischner et al., 2006).

REFERENCES

Abramowitz, M., and I. Stegun, 1972, Handbook of mathematical functions with formulas, graphs, and mathematical tables: U. S. Government Printing Office.

Asanuma, H., H. Nozaki, T. Uhara, H. Niitsuma, R. Baria, and D. Wyborn, 2006, Spatial and temporal distribution of larger seismic events at European and Australian HDR sites: Proceedings, 31st Workshop on Geothermal Reservoir Engineering, Stanford University, http://www.geothermal-energy.org/pdf/IGAstandard/SGW/2006/asanuma.pdf?, accessed 7 May 2011.

Aziz, K., and A. Settari, 1979, Petroleum reservoir simulation: Gulf Publishing Company, Houston, Texas

Baisch, S., R. Vörös, E. Rothert, H. Stang, R. Jung, and R. Schellschmidt, 2010, A numerical model for fluid injection induced seismicity at Soultz-sous-Forêts: International Journal of Rock Mechanics and Mining Sciences & Geomechanics Abstracts, **47**, 3, 405–413.

Baisch, S., R. Weidler, R. Vörös, and R. Jung, 2006, A conceptual model for post-injection seismicity at Soultz-sous-Forêts: GRC Transactions, **30**, 601–605.

Baria, R., R. Jung, T. Tischner, J. Nicholls, S. Michelet, B. Sanjuan, N. Soma, H. Asanuma, B. Dyer, and J. Garnish, 2006, Creation of an HDR reservoir at 5000 m depth at the european HDR project: Proceedings, 31st Workshop on Geothermal Reservoir Engineering, Stanford University, http://www.geothermal-energy.org/pdf/IGAstandard/SGW/2006/baria1.pdf?, accessed 7 May 2011.

Barton, N., S. Bandis, and K. Bakhtar, 1985, Strength, deformation and conductivity coupling of rock joints: International Journal of Rock Mechanics and Mining Sciences & Geomechanics Abstracts, **22**, no. 3, 121–140.

Ben-Zion, Y., 2008, Collective behavior of earthquakes and faults: Continuum-discrete transitions, progressive evolutionary changes, and different dynamic regimes: Reviews of Geophysics, **46**, RG4006.
Ben-Zion, Y., and J. Rice, 1993, Earthquake failure sequences along a cellular fault zone in a three-dimensional elastic solid containing asperity and nonasperity regions: Journal of Geophysical Research, **98**, 14, 109–14, 131.
Bruel, D., 2007, Using the migration of the induced seismicity as a constraint for fractured hot dry rock reservoir modeling: International Journal of Rock Mechanics and Mining Sciences & Geomechanics Abstracts, **44**, 8, 1106–1117.
Bruel, D., and J. Charlety, 2007, Moment-frequency distribution used as a constraint for hydro-mechanical modelling in fracture networks: International Society for Rock Mechanics, 11th ISRM Congress, Portugal.
Bruhn, R., W. Parry, W. Yonkee, and T. Thompson, 1994, Fracturing and hydrothermal alteration in normal fault zones: Pure and Applied Geophysics, **142**, no. 3-4, 609–644.
Caine, J., J. Evans, and C. Forster, 1996, Fault zone architecture and permeability structure: Geology, **24**, 1025–1028.
Charlety, J., N. Cuenot, L. Dorbath, C. Dorbath, H. Haessler, and M. Frogneux, 2007, Large earthquakes during hydraulic stimulations at the geothermal site of Soultz-sous-Forêts: International Journal of Rock Mechanics & Mining Sciences, **44**, 8, 1091–1105.
Cornet, F.H., and T. Bérard, 2003, A case example of integrated stress profile evaluation, in rock stress, K. Sugawara, Y. Obara, and A. Sato, eds., A. A. Balkema Publishers.
Cornet, F., Th. Bérard, and S. Bourouis, 2007, How close to failure is a granite rock mass at a 5 km depth?: International Journal of Rock Mechanics & Mining Sciences, **44**, no. 1, 47–66.
Crouch, S. L., and A. M. Starfield, 1983, Boundary element methods in solid mechanics: George Allen & Unwin Ltd..
Deng, S., R. Podgorney, and H. Huang, 2011, Discrete element modeling of rock deformation, fracture network development and permeability evolution under hydraulic stimulation: Proceedings, 36th Workshop on Geothermal Reservoir Engineering, Stanford University, http://www.geothermal-energy.org/pdf/IGAstandard/SGW/2011/deng.pdf?, accessed 7 May 2011.
Dezayes, C., A. Genter, and B. Valley, 2010, Structure of the low permeable naturally fractured geothermal reservoir at Soultz: Comptes Rendus Geoscience, **342**, 7-8, 517–530.
Dieterich, J., 1979, Modeling of rock friction 1. Experimental results and constitutive equations: Journal of Geophysical Research, **84**, 2161–2168.
Dieterich, J., 2007, Applications of rate- and state-dependent friction to models of fault slip and earthquake occurrence: *in* H. Kanamori, ed., Treatise on Geophysics, vol. **4**, Elsevier, 107–129, http://www.sciencedirect.com/science/referenceworks/9780444527486, accessed 7 May 2011.
Dieterich, J., and B. Kilgore, 1994, Direct observation of frictional contacts: New insight for state-dependent properties: Pure and Applied Geophysics, **143**, 283–302.
Esaki, T., S. Du, Y. Mitani, K. Ikusada, and L. Jing, 1999, Development of a shear-flow test apparatus and determination of coupled properties for a single rock joint: International Journal of Rock Mechanics and Mining Sciences & Geomechanics Abstracts, **36**, 5, 641–650.
Evans, K., A. Genter, and J. Sausse, 2005b, Permeability creation and damage due to massive fluid injections into granite at 3.5 km at Soultz: 1. Borehole Observations: Journal of Geophysical Research, **110**, B04203.
Evans, K., H. Moriya, H. Niitsuma, R. Jones, W. Phillips, A. Genter, J. Sausse, R. Jung, and R. Baria, 2005a, Microseismicity and permeability enhancement of hydrogeologic structures during massive fluid injections into granite at 3 km depth at the Soultz HDR site: Geophysical Journal International, **160**, 388–412.
Genter, A., X. Goerke, J.-J. Graff, N. Cuenot, G. Krall, M. Schindler, and G. Ravier, 2010, Current status of the EGS Soultz geothermal project (France): Proceedings, World Geothermal Congress, Bali, Indonesia, http://www.geothermal-energy.org/pdf/IGAstandard/WGC/2010/3124.pdf?, accessed 7 May 2011.
Genter, A., H. Traineau, B. Ledésert, B. Bourgine, and S. Gentier, 2000, Over 10 years of geological investigations within the HDR Soultz project, France: Proceedings, World Geothermal Congress, Kyushu — Tohoku, Japan, http://www.geothermal-energy.org/pdf/IGAstandard/WGC/2000/R0710.PDF?, accessed 7 May 2011.
Ghassemi, A., and S. Tarasovs, 2006, Fractures slip and opening in response to fluid injection into a geothermal reservoir: Proceedings, 31st Workshop on Geothermal Reservoir Engineering, Stanford University, http://www.geothermal-energy.org/pdf/IGAstandard/SGW/2006/ghassemi.pdf?, accessed 7 May 2011.
Gomberg, J., M. Belardinelli, M. Cocco, and P. Reasenberg, 2005, Time-dependent earthquake probabilities: Journal of Geophysical Research, **110**, B05S04.
Griffith, W. A., P. Sanz, and D. Pollard, 2009, Influence of outcrop scale fractures on the effective stiffness of fault damage zone rocks: Pure and Applied Geophysics, **166**, 1595–1627.
Hanks, T., and H. Kanamori, 1979, A moment magnitude scale: Journal of Geophysical Research, **84**, 2348–2350.
Häring, M., F. Ladner, U. Schanz, and T. Spillman, 2007, Deep heat mining basel, preliminary results: Proceedings, European Geothermal Conference, http://www.geothermal-energy.org/pdf/IGAstandard/EGC/2007/184.pdf, accessed 7 May 2011.
Hayashi, K., and H. Abe, 1982, Opening of a fault and resulting slip due to injection of fluid for the extraction of geothermal heat: Journal of Geophysical Research, **87**, 1049–1054.
Hayashi, K., and H. Abe, 1983, Opening of a fault and resulting slip due to injection of fluid for the extraction of geothermal heat 2. Further details: Journal of Geophysical Research, **88**, 8299–8304.
Healy, J. W., D. Rubey, D. Griggs, and C. Raleigh, 1968, The denver earthquakes: Disposal of waste fluids into a deep well has triggered earthquakes near Denver, Colorado: Science, **161**, 1301–1310.
Hettkamp, T., J. Baumgärtner, R. Baria, A. Gérard, T. Gandy, S. Michelet, and D. Teza, 2004, Electricity production from hot rocks: Proceedings, Twenty-Ninth Workshop on Geothermal Reservoir Engineering, Stanford University, http://www.geothermal-energy.org/pdf/IGAstandard/SGW/2004/Hettkamp.pdf, accessed 7 May 2011.
Hillers, G., Y. Ben-Zion, and P. Mai, 2006, Seismicity on a fault controlled by rate- and state-dependent friction with spatial variations of the critical slip distance, Journal of Geophysical Research, **111**, B01403.
Holmgren, M., 2007, Xsteam: Water and steam properties according to IAPWS IF-97, www.x-eng.com, accessed 7 May 2011.
Hsieh, P., and J. Bredehoeft, 1981, A reservoir analysis of the Denver earthquakes: A case of induced seismicity: Journal of Geophysical Research, **86**, 903–920.
Jaeger, J. C., N. G. W. Cook, and R. W. Zimmerman, 2007, Fundamentals of rock mechanics: Blackwell Publishing.
Karimi-Fard, M., L. J. Durlofsky, and K. Aziz, 2004, An efficient discrete-fracture model applicable for general-purpose reservoir simulators: paper SPE 88812, presented at the 2003 SPE Reservoir Simulation Symposium, Houston, TX, http://www.onepetro.org/mslib/servlet/onepetropreview?id=00088812&soc=SPE, accessed 7 May 2011.
Kim, J., H. A. Tchelepi, and R. Juanes, 2011, Stability, accuracy, and efficiency of sequential methods for coupled flow and geomechanics: paper SPE 119084, presented at the 2009 SPE Reservoir Simulation Symposium, The Woodlands, TX, (SPE Journal, in press), http://www.spe.org/ejournals/jsp/journalapp.jsp?pageType=Preview&jid=ESJ&mid=SPE-119084-PA, accessed 7 May 2011.
Kohl, T., and T. Mégel, 2007, Predictive modeling of reservoir response to hydraulic stimulations at the European EGS site Soultz-sous-Forêts: International Journal of Rock Mechanics & Mining Sciences, **44**, no. 8, 1118–1131.
Lapusta, N., 2001, Elastodynamic analyses of sliding with rate and state friction: Ph.D. thesis Harvard University, http://esag.harvard.edu/lapusta/Lapusta_phd_thesis.pdf, accessed 7 May 2011.
Lee, H. S., and T. F. Cho, 2002, Hydraulic characteristics of rough fractures in linear flow under normal and shear load: Rock Mechanics and Rock Engineering, **35**, no. 4, 299–318.
Lockner, D., H. Tanaka, H. Ito, R. Ikeda, K. Omura, and H. Naka, 2009, Geometry of the Nojima fault at Nojima-Hirabayashi, Japan — i. A simple damage structure inferred from borehole core permeability: Pure and Applied Geophysics, **166**, 1649–1667.
Majer, E., R. Baria, M. Stark, S. Oates, J. Bommer, B. Smith, and H. Asanuma, 2007, Induced seismicity associated with enhanced geothermal systems: Geothermics, **36**, 3, 185–222.
Marone, C., C. B. Raleigh, and C. H. Scholz, 1990, Frictional behavior and constitutive modeling of simulated fault gouge: Journal of Geophysical Research, **95**, 7007–7025.
McClure, M., and R. N. Horne, 2010, Numerical and analytical modeling of the mechanisms of induced seismicity during fluid injection: GRC Transactions, **34**, 381–396.
Morrow, C., and J. Byerlee, 1989, Experimental studies of compaction and dilatancy during frictional sliding on faults containing gouge: Journal of Structural Geology, **11**, no. 7, 815–825.
Rachez, X., and S. Gentier, 2010, 3D-hydromechanical behavior of a stimulated fractured rock mass: Proceedings, World Geothermal Congress, Bali, Indonesia, http://www.geothermal-energy.org/pdf/IGAstandard/WGC/2010/3152.pdf, accessed 7 May 2011.
Rahman, M. K., M. M. Hossain, and S. S. Rahman, 2002, A shear-dilation based model for evaluation of hydraulically stimulated naturally fractured reservoirs: International Journal for Numerical and Analytical Methods in Geomechanics, **26**, 5, 469–497.
Rice, J., 1993, Spatio-temporal complexity of slip on a fault: Journal of Geophysical Research, **98**, 9885–9907.
Ruina, A., 1983, Slip instability and state variable friction laws: Journal of Geophysical Research, **88**, 10, 359–10, 370.

Segall, P., 2010, Earthquake and volcano deformation: Princeton University Press.
Segall, P., and J. Rice, 1995, Dilatancy, compaction, and slip instability of a fluid-infiltrated fault: Journal of Geophysical Research, **100**, 22, 115–22, 171.
Segall, P., A. Rubin, and J. Rice, 2010, Dilatant strengthening as a mechanism for slow slip events: Journal of Geophysical Research, **115**, B12305.
Shapiro, S., P. Audigane, and J. –J. Royer, 1999, Large scale in-situ permeability tensor of rocks from induced microseismicity: Geophysical Journal International, **137**, 207–213.
Shapiro, S., and C. Dinske, 2009, Fluid-induced seismicity: Pressure diffusion and hydraulic fracturing: Geophysical Prospecting, **57**, 2, 301–310.
Stein, S., and M. Wysession, 2003, An introduction to seismology, earthquakes, and earth structure: Blackwell Publishing, Ltd..
Tester, J., ed., 2007, The Future of Geothermal Energy: Impact of Enhanced Geothermal Systems (EGS) on the United States in the 21st Century: MIT Report, http://geothermal.inel.gov/publications/future_of_geothermal_energy.pdf, accessed 7 May 2011.
Tischner, T., M. Pfender, and D. Teza, 2006, Hot dry rock projekt Soultz: Erste phase der erstellung einer wissenschaftlichen pilotanlage: Final Project Report, http://www.bgr.bund.de/DE/Themen/Energie/Downloads/soultz_abschlussbericht.pdf?__blob=publicationFile&v=2, accessed 7 May 2011.
Valley, B., and K. Evans, 2007, Stress state at Soultz-sous-Forêts to 5 km depth from wellbore failure and hydraulic observations: Proceedings, Thirty-Second Workshop on Geothermal Reservoir Engineering, Stanford University, http://www.geothermal-energy.org/pdf/IGAstandard/SGW/2007/valley.pdf, accessed 7 May 2011.
Weidler, R., 2000, Hydraulic stimulation of the 5 km deep well gpk-2: BGR Report, 17 August 2000.
Wibberley, C., G. Yielding, and G. Di Toro, 2008, Recent advances in the understanding of fault zone internal structure: A review:, from Wibberley, et al., eds., The internal structure of fault zones: Implications for mechanical and fluid-flow properties: Geological Society, Special Publications, **299**, 5–33.
Willis-Richards, J., K. Watanabe, and H. Takahashi, 1996, Progress toward a stochastic rock mechanics model of engineered geothermal systems: Journal of Geophysical Research, **101**, 17, 481–17, 496.
Yamashita, T., 1999, Pore creation due to fault slip in a fluid-permeated fault zone and its effect on seismicity: Generation mechanism of earthquake swarm: Pure and Applied Geophysics, **155**, 625–647.
Zoback, M., 2007, Reservoir geomechanics: Cambridge University Press.